Defect induced laser damage in oxide multilayer coatings for 248 nm

M. Reichling [a,*], A. Bodemann [b], N. Kaiser [b]

[a] *Fachbereich Physik, Freie Universität Berlin, Arnimallee 14, 14195 Berlin, Germany*
[b] *Fraunhofer-Institut für Angewandte Optik und Feinmechanik, Schillerstraße 1, 07745 Jena, Germany*

Abstract

Photothermal displacement microscopy is used for the detection of μm-sized defects in Al_2O_3/SiO_2 multilayer coatings highly reflective for 248 nm. It is shown that for high quality coatings the global (averaged over several cm^2) laser-induced damage threshold for coatings of different quality is determined by the density and absorption strength of the light absorbing defects. This is confirmed by a measurement of local (averaged over 0.01 mm^2) damage thresholds with the pulsed photoacoustic mirage technique allowing a direct correlation of local damage with photothermally detected thin film defects. An analysis of laser-damaged spots reveals damage-craters of 13 μm diameter at the onset of detrimental irradiation effects. The formation of these craters is explained by a thermoelastic model describing the tensile stress in the film system resulting from evaporation of a defect located at the interface between thin film and substrate. © 1998 Elsevier Science S.A. All rights reserved.

1. Introduction

Ultraviolet (UV) light from excimer laser systems is today used for a variety of important technological applications. One of the most prominent application is material processing where high energy pulses are used for precision micromachining [1] and lithography [2]. The equipment used for producing, guiding, shaping and focusing of the UV laser beams normally involves an optical system with a large number of coated surfaces. These optical components have to withstand millions of high intensity pulses and, therefore, the laser damage threshold is one of the most important figures of merit for optical coatings in high power laser applications. Light absorption by the thin film material [3] and defect-related absorption [3,4] is the limiting factor for the optics especially in the UV spectral region. With state of the art technology, damage thresholds of more than 20 J/cm^2 at 248 nm for ns-laser pulses can presently be obtained [5,6] and the main problem in thin film manufacturing is to reduce defect absorption that can reduce the local damage threshold considerably. So far, however, this problem has mostly been studied for infrared laser light [4] while the damage behaviour may be very

different when working in the UV [7] where local and non-local damage phenomena have been observed [8]. Some general studies attacked the question of localised defect absorption and recently it has been shown that, e.g. nodular defects may play an important role for infrared multilayer coatings [9]. A scanning force microscopy study demonstrated that damage occurring at sites of nodular defects may, in fact, define the damage threshold [10]. Minute local absorption from defects has also been detected by several photothermal techniques. Recent work includes photothermal mirage microscopy [11] and photothermal displacement microscopy [12].

With the present work we try to elucidate the role of absorbing defects in Al_2O_3/SiO_2 multilayer highly reflective (HR) coatings for 248 nm in some detail and aim to establish a correspondence between thin film defects and the apparent damage threshold of the coating. The ultimate goal of such studies is to develop a predictive method for the determination of the laser resistivity with non-destructive methods. This contribution is a first step in this direction since for the first time we directly correlate the absorption strength of thin film defects with individual damage events at the respective location. To accomplish this task we combine results from two photothermal techniques, namely, the photothermal displacement technique [13] for defect detection and the pulsed photoacoustic

* Corresponding author. Fax: +49-30-838-6059; e-mail: reichling@matth1.physik.fu-berlin.de.

mirage technique [14] for the measurement of damage thresholds.

First, defects are localised with μm-resolution and characterized with respect to their size, distribution and relative absorption strength with photothermal displacement absorption microscopy, a technique that has been shown to be well suited for optical thin film studies since it combines ultra-high sensitivity with μm-resolution [15]. However, due to the very complicated absorption profile and thermoelastic response of a multilayer thin film system, displacement measurements are difficult to calibrate absolutely [16,17] and throughout this paper we present only relative absorption data. In a second step the global (i.e., averaged over several cm^2) laser-damage thresholds F_T for the coatings are determined by conventional damage testings [18] and the photoacoustic mirage technique [19] and the damage threshold is discussed in view of the defect mapping results. The last step involves a direct correlation between photothermally localized defects and damage centers appearing after irradiation with excimer-laser light with fluences below the global damage threshold. The defect-related nature of such damage centers is verified by an analysis of their morphology with optical and electron microscopy. A prominent manifestation of defect-related laser damage is the formation of ablation craters at sites of enhanced light absorption. The formation of such craters is discussed in terms of a thermoelastic model explaining the ejection of cone-shaped fragments of the thin film layer stack.

2. Samples

Samples were Al_2O_3/SiO_2 multilayer highly reflective coatings for 248 nm prepared by electron beam evaporation on SQ1 quartz substrates. The coatings design was (air)2L(HL)^{n}H(substrate); i.e., they consisted of typically $n = 20$ alternating $\lambda/4$ layers of low (L) and High (H) refractive materials and were covered by a $\lambda/2$ protection layer of SiO_2 on top of the stack. Various coating qualities were obtained by evaporation and handling of substrates in different environments. High quality samples were produced in clean rooms that have been in operation for several years and guaranteed lowest levels of contamination. Deposition has been performed in a BALZERS BAK 640 coating chamber equipped with a refrigerator cryopump and a LN$_2$ cooled Meissner trap. The coating and substrate cleaning equipment was under class 10.000–1.000 clean room conditions. Film thicknesses and deposition rates were controlled by an optical monitor at 248 nm and a quartz oscillator, respectively. Both Al$_2$O$_3$ (99.5% Patinal) and SiO$_2$ (99.89% Patinal) have been evaporated reactively from electron beam evaporators (6 kV, 15 kW total power) with rotary crucibles and Mo-liners. Substrate temperature was about 570 K. No further energy input by ion or plasma sources was made to avoid additional absorption losses. To obtain lowest levels of contamination special care was taken during preparation of the substrates (SQ1 Glaswerke Jena). The substrate cleaning procedure included pre-cleaning steps in ultrasonic baths (Optical 2S and Optical 6), post-cleaning by hand with alcohol and acetone (cotton wool) and overcoating with Opti-Clean. The Opti-Clean was removed some minutes before starting the deposition. For comparison lower quality coatings were evaporated in a conventional oil diffusion pumped vacuum chamber with a LN$_2$ baffle. However, the design and all other preparation conditions were identical to those applied for the preparation of the high quality coatings.

To test mechanical properties of the dielectric films involved in the coating systems, we evaporated single films of various thickness onto silicon substrates using conditions similar to those used for the preparation of the optical coatings. The intrinsic stresses of these films were determined with a Tencor instrument by a substrate bending technique. For SiO$_2$ layers of a thickness below 100 nm we observed compressive stress of several hundred MPa while the compressive stress in Al$_2$O$_3$ was about 100 MPa. HfO$_2$ layers exhibited tensile stress of typically 300 MPa.

Global damage thresholds F_T for a wavelength of 248 nm were determined in a standard testing facility described elsewhere [20]. In the following we report on a set of samples representing coatings with inferior quality ($F_T < 1$ J/cm^2), standard quality ($F_T = $ some J/cm^2) and high quality ($F_T > 15$ J/cm^2) that have been used for a detailed photothermal and damage analysis. The main parameters of these samples are compiled in Table 1. Samples **A**, **B** and **C** were used for an analysis of density, strength and spatial distribution of defects by photothermal microscopy. A detailed investigation of damaged spots was performed on samples **D** and **E** with photothermal and interference microscopy and with higher resolution by scanning electron microscopy (SEM). Finally, global and local damage thresholds have been measured for the high quality samples **F** and **G** and the location of damaged spots was correlated with an absorption map previously obtained by

Table 1
Compilation of design and damage data for the HR coatings

Sample	Number of layers	Damage threshold (J/cm^2)
A	49	0.6
B	41	3.0
C	41	15.9
D	49	2.0
E	41	n.a.
F	41	22.5
G	41	19.0
H	21 (HfO$_2$/SiO$_2$)	n.a.

All samples were Al$_2$O$_3$/SiO$_2$ (except sample **H**) multilayer systems consisting of $\lambda/4$ layers (248 nm) and were covered with a $\lambda/2$ SiO$_2$ protective overcoat. Damage data refers to global damage thresholds determined for 248 nm/20 ns laser light.

photothermal microscopy. Sample **H** was a HfO_2/SiO_2 multilayer system designed as an example to demonstrate how a variation in material properties may yield dramatic changes in the observed damage phenomena.

3. Photothermal defect mapping

Photothermal microscopy measurements on samples **A**, **B** and **C** were performed with a photothermal apparatus described in detail elsewhere [12]. The instrument was operated in the displacement mode at 1 kHz modulation frequency with a lateral resolution of about 10 μm determined by the focal diameters of pump and probe beam. Images shown in this paper represent the variation of the amplitude of the photothermally induced in-plane deflection of the probe beam for two-dimensional scans over the sample surface. Photothermal displacement scanning provides a map of thin film absorption at the pump laser wavelength of 514 nm and colour coding of the signal amplitude allows a comparison between the absorption strength of different samples since care was taken to always work in the maximum of the photothermal displacement profile. However, the photothermal microscope was not calibrated in absolute units of absorbed energy. Except for a few obvious surface contaminations the absorption centers could not be identified by optical microscopy.

Fig. 1 shows the amplitude images over regions of 800×800 μm^2 for samples **A**, **B** and **C**, respectively. Distinct differences appear in the images for samples of different quality. The image for sample **A** reveals a strong background absorption over the entire scanned area and a large number of randomly distributed defects varying in size and absorption strength. Defect density appears to be similar for sample **B**, however, the background signal is much smaller compared to the absorption peak amplitudes. Note that the colour codes of the images in Fig. 1 have been scaled differently to obtain an optimum contrast for the defects, however, the mean background amplitude is higher by a factor of 35 for sample **A** than for sample **B**. A completely different result is found for the high quality sample **C**. Here, the background absorption was extremely small and only a very small number of weakly absorbing defects could be identified. Additionally these defects exhibited different shapes and seem to be of a different nature than those from the other samples. The marked differences in defect absorption found between samples **B** and **C** are demonstrated in Fig. 2 where smaller sections of images from Fig. 1 are displayed with the same expanded colour coding. These images were obtained by scanning with higher resolution and sensitivity and they allow an insight into subtle variations of local absorption. For sample **B** the increased sensitivity yields the appearance of numerous weakly absorbing defects additional to the strongly absorbing ones while they are not present in sample **C** where the noisy background indicates extremely small homogeneous absorption close to the detection limit of the photothermal microscope used for this series of measurements.

To investigate defect properties in more detail a statistical analysis was applied to the absorption images of samples **A** and **B**. A comparison of the defect size distributions is shown in Fig. 3. It was found that the total number of defects was about equal for both samples, however, the size distributions differed considerably. While defects are about equally distributed for sample **B**, a distinct peak of defects between 10 and 30 μm was found for the lowest quality sample **A**.

In summary we found that there is a clear correlation between defect properties (measured at 514 nm) of the investigated highly reflecting coatings and the laser damage threshold determined at the wavelength of maximum reflection (248 nm). Although, the least quality coating **A** also has a strong homogeneous background absorption, the strong interaction with the laser light and consequently the damage threshold is determined by localized defects. In this sample a certain class of strongly absorbing defects with a size of 10 to 30 μm seems to be most relevant for the detrimental light-thin film interaction. In the normal quality sample **B** the situation is similar, however, there a broader variety of defect sizes governs the absorption properties. From this set of measurements it is not clear whether the global damage threshold of the high quality sample **C** is determined by defects or by the intrinsic absorption of the thin film materials. This question will be investigated in more detail in Section 6.3.

4. Damage phenomena

4.1. Massive damage

The manifestations of laser damage were studied on low and standard quality sample since there large area damage

---

Fig. 1. Amplitude images of photothermal scans on samples with different damage thresholds: **A**: 0.6 J/cm^2, **B**: 3.0 J/cm^2, **C**: 15.9 J/cm^2. The colour sequence from black to white represents increasing levels of absorption. To obtain an optimum visibility of defects the colour sequence has been scaled differently for images **A** and **B**; i.e., same colours represent different absorption levels (see text). The squares surrounded by dashed lines are regions displayed in Fig. 2 that have been re-scanned with increased sensitivity and resolution.

Fig. 2. Magnified details from samples **B** and **C**. To enhance visibility of weak absorption centers the brightest colour represents 1/10 of the absorption assigned to the brightest colour in the respective images of Fig. 1.
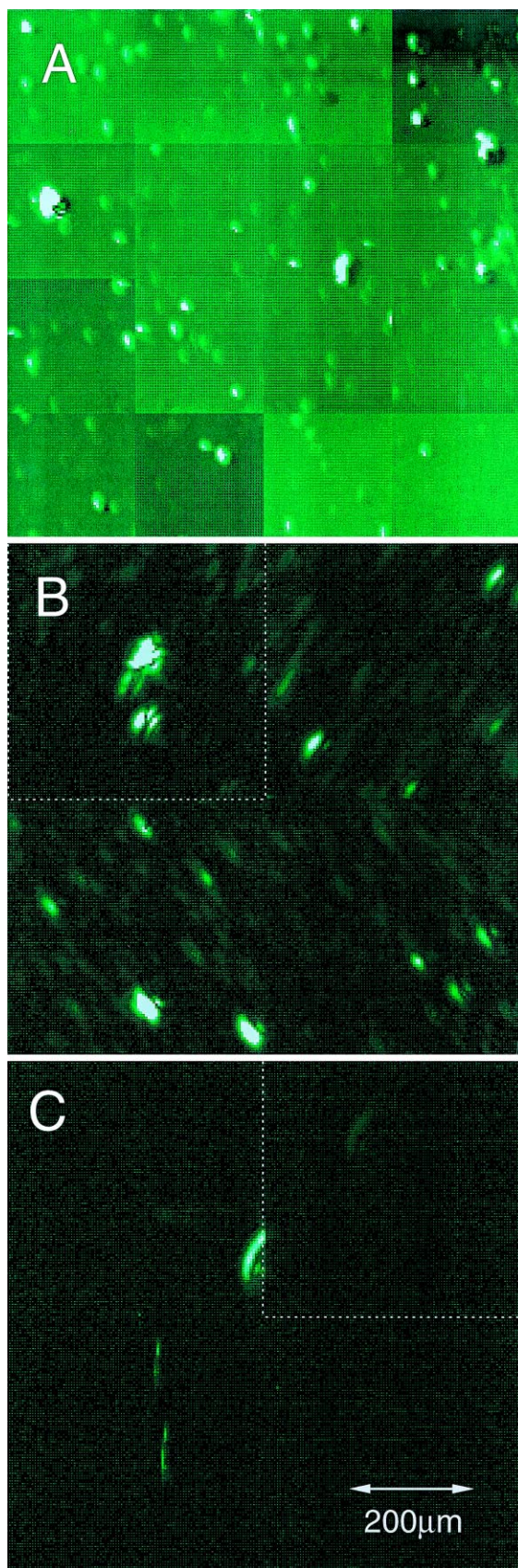
Fig. 1
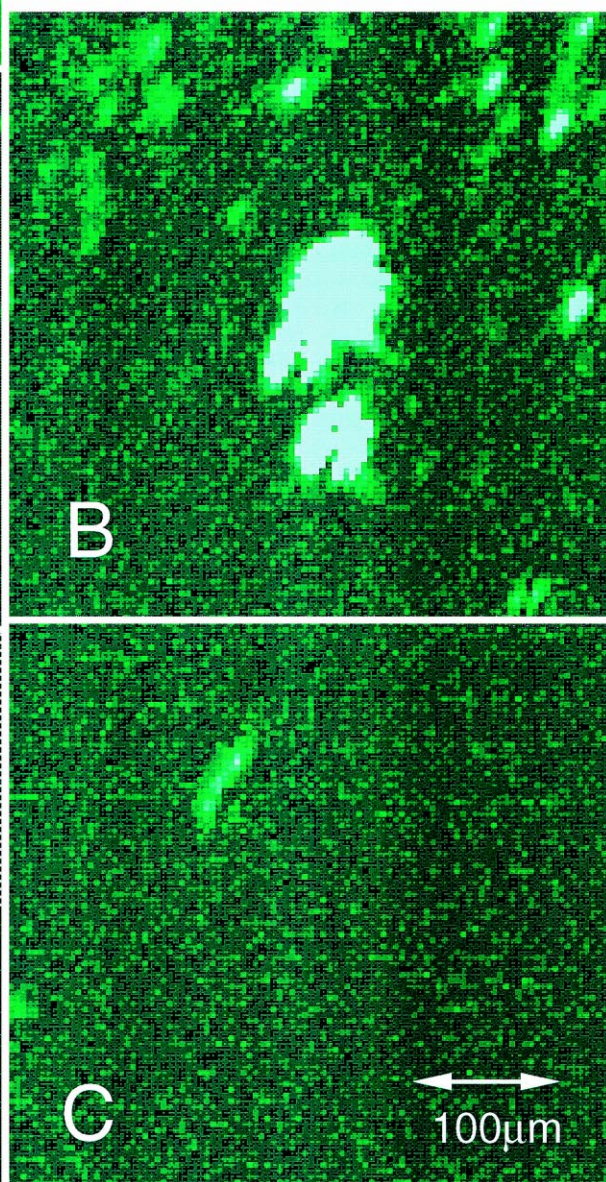
Fig. 2
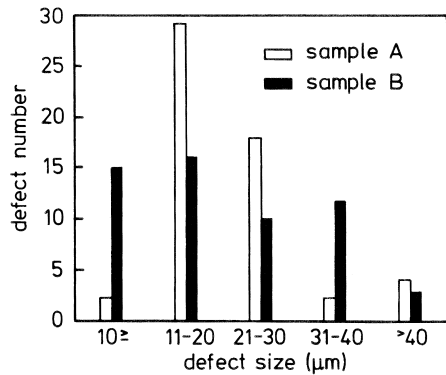
Fig. 3. Statistical analysis of photothermal images on samples **A** and **B** from Fig. 1 with respect to the size of photothermally detected defects.

and defect-related effects can most conveniently be separated. A typical example for damage with a fluence well above the threshold for sample **D** is shown in Fig. 4a. This image is representative for a situation with rather homogeneous absorption where damage morphology is more determined by the laser beam profile than by localized absorptions. It was obtained by interference microscopy in the shearing mode showing steps as a pronounced line with a strong colour contrast [21]. Large areas of thin film material have been ablated leaving behind elliptical terraces following the laser beam profile.

Beside the described large area ablation, Fig. 4b that was obtained under similar conditions than Fig. 4a reveals first hints for defect-initiated damage. The damaged spot contains several small circular craters where the damage extends much deeper into the stack than in the surroundings. Apparently, at these locations the ablation morphology is not determined by the laser beam intensity profile but triggered by localized absorptions. Such phenomena will be described in detail in Section 5.

To explain the predominant terrace structure we assume that the film system is heated by the laser pulse and evaporation starts at the topmost layer over the largest area where the temperature is highest. Since the thermal length [22], i.e. the penetration depth of the heat during the laser pulse, in the Al_2O_3 layers for a 20 ns laser pulse of approximately 20 nm is of the order of the geometrical layer thickness of 37 nm, the in-depth temperature profile is mainly determined by the light intensity decaying with depth. Therefore, the structure of terraces follows the thermal (i.e. intensity) lateral profile of the damaging laser beam. The shearing method allows a determination of the optical thickness of the ablated layers. It was found that the thickness of each terrace was $\lambda/2$, i.e. damage starts with the removal of the SiO_2 protective overcoat and then layers are not ablated individually but in SiO_2/Al_2O_3-pairs. The regular sequence of $\lambda/2$-terraces implies and an EDX-analysis on the terraces [23] confirms that they are terminated by Al_2O_3-layers what is presumably a result of the much higher melting and evaporation temperatures [24]

of Al_2O_3 compared to that of SiO_2. As soon as the evaporation temperature of SiO_2 is exceeded the gas pressure leads to an ejection of the above Al_2O_3 that has already melted at that temperature. The lateral temperature gradient results in a regular ablation pattern with a terrace structure. As shown in the SEM-image of Fig. 4c the edges of the terraces are covered by droplets of molten material with a preferential alignment in radial direction following both, the temperature gradient and the gas flow after evaporation.

The preferential sputtering of layer pairs might additionally be favoured by intrinsic stresses in the individual films that do not compensate each other and result in a sequence of interfaces alternating in low and high adhesion strength. Such phenomena can be detected by an investigation of cross sections of fractured multilayer system that exhibit pronounced terraces in systems with a net stress at the interface [25]. As an example for terrace formation we present a micrograph of a fractured MgF_2/SiO_2 multilayer system. As seen in Fig. 5 the amorphous SiO_2 layers form large terraces while the MgF_2 grown with a columnar microstructure do not. A similar difference in growth has been observed for Al_2O_3/SiO_2 multilayer systems and it was pointed out that also in this case terrace formation is possible [26]. However, the formation of intrinsic stress and, therefore, the adhesion of individual layers strongly depends on the specific preparation conditions for the thin film system [27]. Here it can only be presumed that for the sample used for our damage experiments the adhesion properties were such that an Al_2O_3-terminated surface is the most stable when a destructive stress is applied to the multilayer stack.

4.2. Explosive damage

Localized damage with a completely different damage morphology was found for sample **H** representing a HfO_2/SiO_2-system. Fig. 6 shows local damage at the periphery of a larger damaged spot with a shape somewhat similar to the feature shown in Fig. 4a. As evident from the SEM-image, here melting is of minor importance but damage is dominated by large flakes of thin film material delaminated from the layer underneath. Apparently the center region of the crater has been strongly heated by an absorbing defect resulting in the evaporation of thin film material while the surrounding regions are much less heated and damaged by elastic interactions only. The bending of the flakes with remaining contact to the coating indicates that in this case delamination is induced by the gas pressure of material evaporated from the crater in the center. In the case of a thin film system involving HfO_2, this appears to be a natural scenario since the melting temperature of HfO_2 is well above the evaporation temperature of SiO_2. Consequently, damage is much less regular than in the previously discussed case and the process is
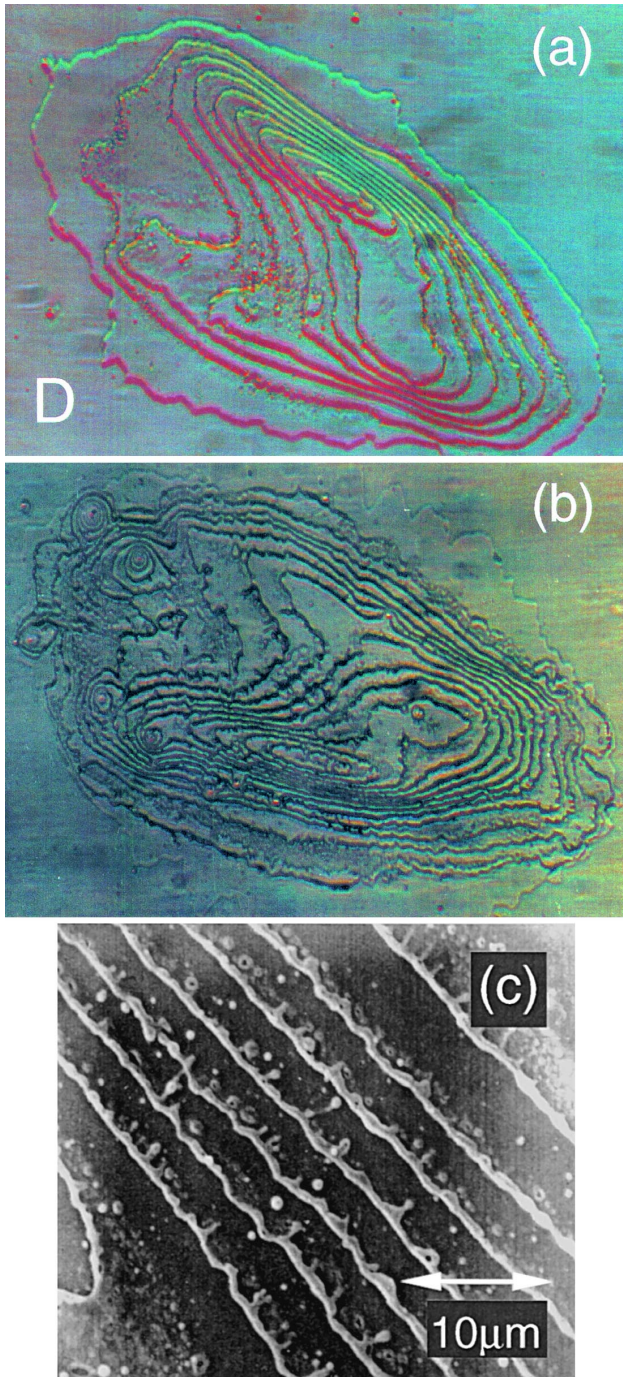
Fig. 4. (a) Interference microscopy (shearing method) image showing catastrophic damage on sample **D** after irradiation with a fluence well above the damage threshold. (b) Shearing microscopy image obtained at another damage site on the same sample. (c) SEM image of a detail from Fig. 4a showing evidence for melting at the edges of ablated layers.

governed by elastic and adhesion properties of the HfO_2-film rather than by the melting temperature.

4.3. Large area damage

Thin film delamination due to thermoelastic stress has also been detected around damage spots on the
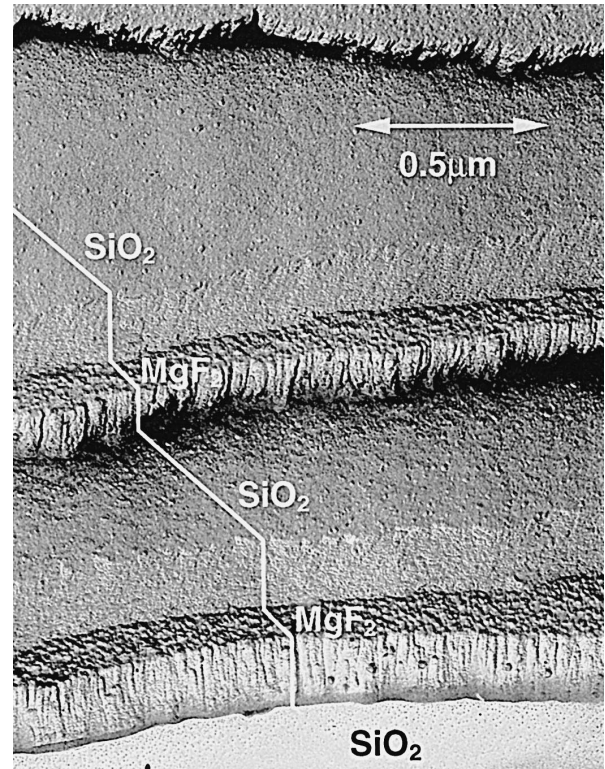
Fig. 5. Cross-section of a MgF_2/SiO_2 multilayer system ($\lambda/2$ for 530 nm) demonstrating the formation of terraces due to different adhesion at alternating interfaces. The micrograph was obtained using a Pt/C replica technique described in Ref. [26].

Al_2O_3/SiO_2-sample **E**. However, in this case the delamination was extended over a very large area but so weak that it could not be detected by (electron) microscopy but only by photothermal imaging. To perform measurements independent of the optical properties of the film and to yield a high photothermal amplitude, samples were sputtered with a 50 nm Pt overlayer after the damaging laser
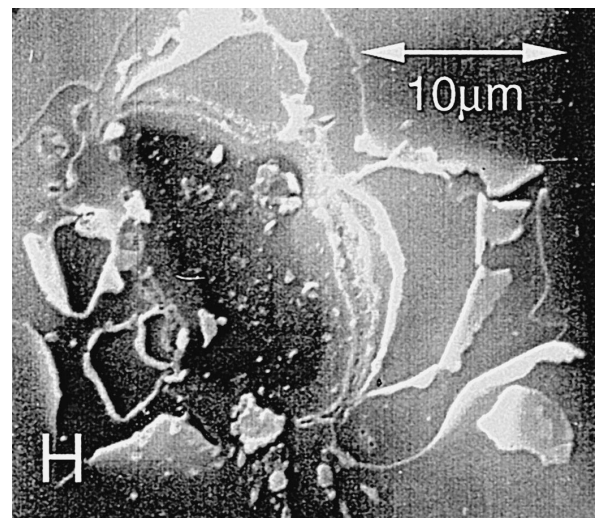
Fig. 6. Massive damage induced by defect absorption in the HfO_2/SiO_2 multilayer sample **H**.
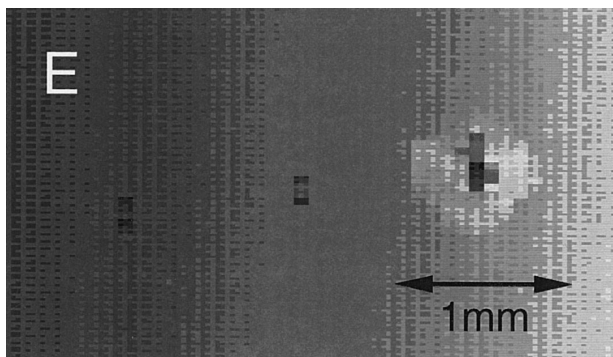
Fig. 7. Large-area photothermal image (brighter shading represents higher signal amplitude) of sample **E** after backside irradiation at three spots with fluences of 0.10, 0.11 and 0.26 J/cm^2 (from left to right). The smooth gradient apparent over the entire image is an experimental artifact resulting from a small misalignment of the sample.

irradiation. It was checked by reflectivity scans that the optical response of the sputtered samples was perfectly homogeneous except at spots of laser damage where scattering caused optical losses. For reasons given below during this measurement the sample was irradiated from the back side through the substrate with three different fluences of 248 nm laser light. The amplitude image of a large-scale photothermal displacement scan over a surface area including all three spots is shown in Fig. 7. In this image the laser damage by the beam with an elliptical profile can be identified in areas of reduced signal amplitude. However, each damaged spot is surrounded by a halo of enhanced signal amplitude. The signal increase in these regions that have not been irradiated by the excimer laser as well as the diameter of the halo obviously depend on the fluence of the damaging light. We interpret the halo as a region where the film has been micro-delaminated by thermoelastic stress acting during the explosion in the damage center. The photothermal displacement contrast is a result of the reduced mechanical contact of the film system to the substrate (or the reduced contact between layers) yielding an increase in signal amplitude.

5. Defect-related damage

5.1. Onset of damage

Prior to photothermal imaging the damage spot on sample **E** with the smallest fluence was investigated with interference and scanning electron microscopy since it revealed interesting defect-related phenomena at the onset of damage. One hypothesis for the explanation of thin film defects in low and standard quality samples was the assumption that the strongest absorptions result from contaminations resting on the substrate prior to thin film deposition. Such contaminations may have considerably large absorptions [11] and are unavoidable unless extreme care is taken during substrate handling. To specifically

address these defects it is very convenient to irradiate the sample from the back side and thus create an electric field distribution with a maximum at the interface between substrate and thin film system; i.e. exactly at the assumed location of the substrate contaminants. In fact, in this way it was possible to detect such defects by individual damage events and damage occurred in standard quality samples at a fluence level as low as 0.1 J/cm^2. The typical damage scenario obtained on sample **E** under these conditions is shown in Fig. 8a. The damaged spot again resembles the elliptical beam profile, however, in contrast to the high intensity irradiations from Fig. 4, interference microscopy now shows a random distribution of equally sized damage craters representing the locations of defects over the entire illuminated spot where the crater density is not necessarily correlated with the intensity profile. Only in the maximum of the intensity distribution it is found that craters have a tendency towards a larger size and merge together to form more irregularly shaped damage spots. As shown above, such type of defect-induced damage craters can also result from front-side illumination, however, due to the much weaker electrical field acting at the interface in this case such events are much rarer and restricted to very highly absorbing defects. However, crater damage has also been found for very high quality coatings illuminated with high fluences. In these coatings the layer stack can withstand the laser light that has enough intensity at the interface to evaporate absorbing defects there.

To study the phenomenon in more detail, individual craters have been investigated by SEM. Examples are presented in Fig. 8b and c. It was found that all craters had the same outer diameter of 13 μm and the crater bottom where ablation occurred through the entire stack down to the substrate had a diameter of 6.5 μm. The center of the crater was marked by a small mould while the rest of the bottom plane appeared to be rather smooth. Clear indications for melting of thin film material could be detected at the rim of the crater bottom with melting droplets extending upward over some layers while most of the layers were cut in precisely circular shape forming a cone around the circular bottom plane. The crater walls had a well defined angle with respect to the surface normal common to all craters and this preferential orientation was found to be rather stable. This is impressively visualized in Fig. 8c where two craters in close proximity overlap without any disturbance or irregularity in the plane where they merge. Increasing laser intensity yielded a larger number and merging of craters also in the periphery of the laser beam profile; i.e. it was possible to produce damage by addressing weaker absorption centers.

On first sight this crater damage has a strong resemblance to damage resulting from nodular defects forming similar cones [28]. However, a careful analysis of the damage morphology and the sample surface prior to and after laser irradiation excludes this interpretation. First, the geometrical parameters like cone diameter and crater depth
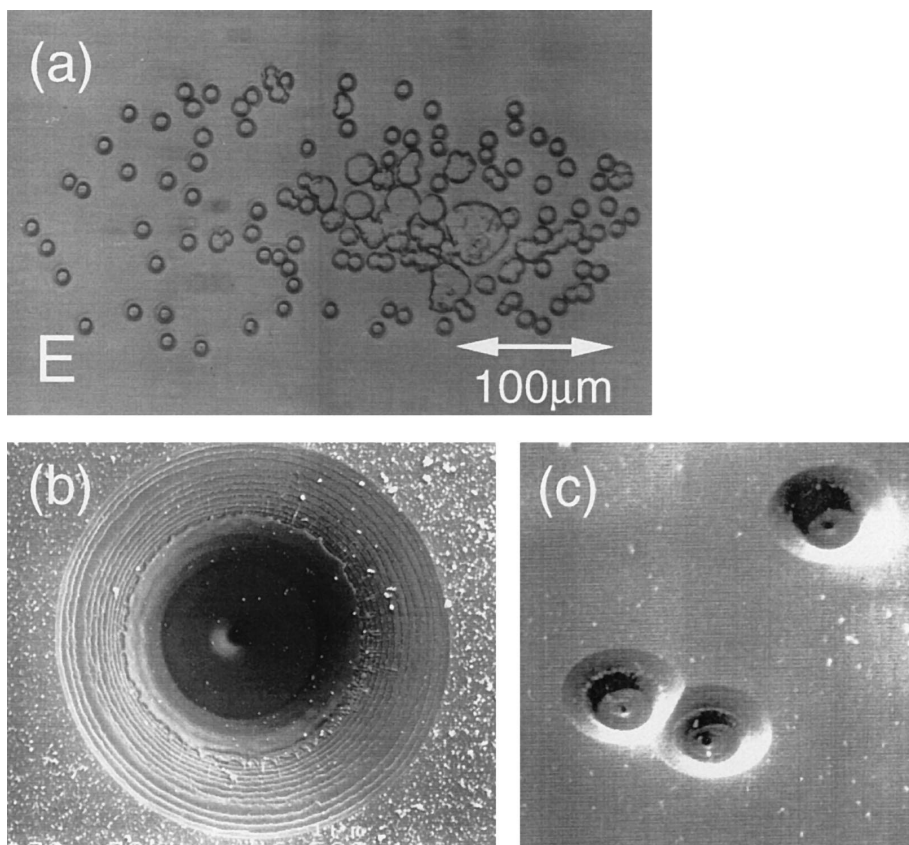
Fig. 8. (a) Interference microscopy image of damage craters resulting from backside irradiation of sample **E** at the onset of defect-induced damage (lowest intensity damage spot from Fig. 7). (b) Detailed view of a damage crater obtained by SEM. (c) SEM micrograph demonstrating the formation of overlapping craters. All craters shown have an outer diameter of 13 μm.

of ejection cones resulting from nodules obey certain relations that do not apply to the craters observed here. Second, the center plateau found in our damage sites has never been observed for nodules. Third, searching thoroughly we could not find any indications that nodular defects are a major phenomenon in our coatings. By systematically rastering samples with high-resolution SEM and atomic force microscopy we found only extremely few surface elevations that could be interpreted as nodules and the apparent density of defects is incompatible with that found, e.g. in Fig. 8a. In a recent study we directly correlated photothermally detected absorption defects in a high quality multilayer coating with the surface structure at the respective locations investigated by scanning force microscopy [29]. It was found that the defects had a lateral dimension of typically 1 to 2 μm and an elevation of about 10 nm was found at the stack surface. These findings clearly exclude nodules as the origin of damage in our case.

5.2. Crater formation

To explain the formation of craters qualitatively several conclusions can be drawn from the experimental evidence and here we present a model for the process that is

sketched in Fig. 9. Since nodules are not observed it is clear that the nucleus of damage is an absorbing defect with a height that is small compared to the thickness of a single layer. By the absorbed laser light the vicinity of the defect is heated to a temperature above the evaporation temperature of the lowest lying thin film material. The expanding gas from the sudden evaporation results in a strong stress pulse perpendicular to the sample surface and shearing stress along the layer planes. During the action of this stress the layer stack is lifted off the substrate and bulged and finally the whole stack pops off when the stress exceeds a critical value as evidenced by the sharp edges of the terraces forming the crater walls with their perfectly circular shape. Tearing off the film is facilitated by melting of the first layer (or layers) due to the high interface temperature. The gas pressure does not only eject the cone but also blow away melted material in radial direction leaving behind the smooth substrate surface found at the bottom of the crater. Only at the location of the defect a strong compressive stress acts on the substrate creating the small impression in the heated and plastically deformed substrate. The main feature to be explained is the significance of the diameter of the bottom plane of the crater. This question has recently been addressed for ablation craters produced with 355 nm light that are very similar to
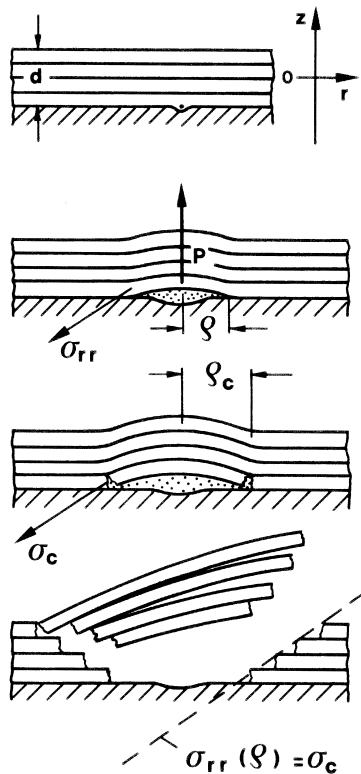
Fig. 9. Schematic illustration of the formation of a damage crater in a multilayer stack by stress induced fracture after laser-evaporation of a defect at the interface between thin film and substrate. The tensile stress σ_{rr} acts in the plane of the layers and is drawn with an inclination for clarity.

what we observed here [30]. In this work an empirical relation between the thickness of single layers and the diameter of the damage craters was given and it was shown by order of magnitude estimates that the ejection process described above is plausible.

5.3. Estimate of critical conditions for crater formation

In the following we extend this work and compile the main formulae governing the elastic response of the layer stack to the stress pulse. An exact quantitative treatment of the crater formation, however, is difficult at present since the absorption properties of the involved defects and the elastic constants of the layer materials are not well known. Numbers given here represent order of magnitude estimates based on the few material constants we found in literature.

For our analysis we assume an inclusion with a size R of 10 nm that for simplicity is assumed to be a spherical particle embedded in a SiO_2 matrix and calculate the temperature rise T when illuminating it with a laser pulse of $J = 10^9$ W/cm^2 intensity:

$$T = \varepsilon_\lambda \frac{JR}{4\kappa} \qquad (1)$$

This formula was derived for a heated inclusion cooled by the matrix by diffusive heat transport [31] and is valid in the small particle approximation that is well justified for nm-sized particles subject to ns-pulses in a matrix with a thermal conductivity of $\kappa = 1.2$ W m^{-1} K^{-1}. We anticipate that in our case the defects have, in fact, a height of about 10 nm but their lateral extension is much larger than that found from the photothermal and SFM studies [29]. This means that the real energy uptake by the defect will be stronger and the assumption of a spherical particle is in the sense of a conservative estimate. The pre-factor ε_λ in Eq. (1) denotes the fraction of incoming light absorbed by the particle and is very difficult to measure or calculate accurately. A rigorous treatment would include a determination of the Mie scattering properties for such small particles [32,33], however, in our case we assume ε_λ to be unity what might result in an over-estimation of the temperature rise. On the other hand, using the SiO_2 bulk value [34] for κ may easily compensate for this since the effective conductivity considering heat flow into thin film materials and a thermal resistance at the interface is anticipated to be much smaller [35].

Under these assumptions we obtain a value of 25 000 K for the temperature rise. Other estimates based on the assumption of radiation cooling [30] yield the same order of magnitude for the inclusion temperature rise under similar conditions. Since the small particle limit heating is mainly determined by the absorbing area, even higher temperatures can be expected when the defect is not a spherical particle but a flat object with a lateral extension larger than the 10 nm radius that has been assumed so far. Therefore, we conclude that in our damage experiments, defects are strongly heated and melting or evaporation will readily occur inducing various types of tensile stress in the vicinity of the inclusion [36].

It has been pointed out, however, that evaporation can only be expected when the confinement of the inclusion by the host is greatly reduced [37], i.e. after material failure occurred. Consequently, for the tensile stress initiating this failure at first place, we assume thermoelastic stress acting due to thermal expansion of the heated inclusion. The stress pulse σ acting at the surface of an inclusion that is subject to rapid heating has been calculated [38] to be:

$$\sigma = \frac{(1-\nu)E}{(1-2\nu)(1-\nu)}\alpha T \qquad (2)$$

where ν, E and α denote the Poisson number, bulk modulus and coefficient of thermal expansion of inclusion and host that are assumed to be the same. Inserting available literature data for thin SiO_2 films of 0.17 and 50 GPa for Poisson ratio and bulk modulus [39] and 0.7×10^{-6}/K for the thermal expansion coefficient [34] yields a stress pulse of 400 MPa for the temperature rise calculated. Again this is a conservative estimate since the values for E

and α are specifically low in the case of SiO_2, e.g. compared to those of Al_2O_3 [34,40].

Such a compressive stress will not result in material failure in the bulk, however, it acts as a tensile stress at the interface between the substrate and the film stack. Damage will be initiated when the tensile stress σ exceeds the critical stress σ_c required to overcome film adhesion. At a perfectly uniform interface between two perfect materials the critical stress only depends on the surface energy γ_s at the interface. The real interface, however, contains imperfections, e.g. interface contaminations as present in our case, that locally concentrate the applied stress and may result in a severe reduction of the critical stress. This effect is commonly described in terms of the Griffith criterion; i.e. material failure will occur if σ_c exceeds the value

$$\sigma_c = \left(\frac{\pi E \gamma_s}{2(1 - \nu^2) \rho} \right)^{\frac{1}{2}} \tag{3}$$

for a penny-shaped flaw with radius ρ embedded in a solid [41] what appears to be the most appropriate geometry in our case. Measured values for the surface energy are not readily available even for surfaces of bulk oxides. For our purpose we use $\gamma_s = 3$ J/m^2 that has been calculated for an Al_2O_3 surface [42]. However, it has to be kept in mind that the quality of adhesion depends to a large degree on the interface layer that forms between film and substrate [27]. For example, for oxide films investigated by a stylus scratch test [43] the critical load for film removal has been found to vary by more than a factor of 30 for different oxide coatings on glass [44]. For an inclusion radius of 10 nm we find a critical stress of 5 GPa that is well above the stress values calculated for the heated inclusion. Assuming, however, an extended defect of 1 μm size yields 400 MPa well matching the assumed thermoelastic stress. In conclusion, it can be stated that a local delamination of the film stack from the substrate is plausible based upon the rough estimate presented here, however, the appearance of damage critically depends on the absorption properties of the defects and the local quality of the interface.

For the following discussion we assume that a small cavity with radius ρ has been formed by local delamination of the layer stack from the substrate in the vicinity of a defect that is assumed to be laser-evaporated (Fig. 9, second frame). Evaporation results in a pressure p acting on the stack of thickness d that is elastically deformed and tensile stress at the interface. The latter promotes further separation of stack and substrate that, according to Eq. (3) becomes increasingly easy with growing cavity radius. In fact, it has been shown by the analysis of the Gibbs free energy of a similar system that growth proceeds infinitely unless it is stopped by an external process [45]. This readily explains large area delamination as e.g. observed in Fig. 7.

In our case the limiting factor is the tensile stress that does not only act at the interface but also inside the stack

and leads to material failure there. To determine the nature of the failure requires an analysis of the stress distribution inside the stack. For simplicity we assume it as a homogeneous plate with radius ρ and thickness d that is clamped over its whole circumference. The displacement u_z of such a plate under the action of a uniform pressure p has been calculated [46] to be

$$u_z(r) = \frac{3(1 - \nu^2)}{16E} \frac{(r^2 - \rho^2)^2}{d^3} p \tag{4}$$

From the displacement field the shear stress components $\sigma_{rr}(r)$ can easily be calculated and it is found that the highest tensile stresses appear at the points of maximum curvature, i.e., in the center of the disk on its top and at the circumference at the bottom. The respective tensile stresses are:

$$\sigma_{rr}{}^{\text{top}}(0) = \frac{3}{4} \frac{(1 + \nu)}{2} \frac{\rho^2}{d^2} p$$

$$\sigma_{rr}{}^{\text{bot}}(\rho) = \frac{3}{4} \frac{\rho^2}{d^2} p$$

Since the Poisson number is always smaller than 0.5, Eq. (5) implies that the maximum tensile stress acts at the circumference. As indicated in the third frame of Fig. 9, damage in form of fracture perpendicular to the surface will be initiated there as soon as the stress exceeds a critical value σ_c defined by the material properties of the first layer. Assuming that the entire spherical inclusion with radius R is evaporated, the pressure in the cavity is estimated using the equation of state for the ideal gas:

$$p_c V_c = \frac{4\pi}{3} R^3 \frac{1}{V_M} \Re \, \Delta T \text{ where } V_c = \frac{\pi}{2} u_c \rho_c^2 \tag{6}$$

Here V_M denotes the molar volume of the inclusion material and $\Re$ is the universal gas constant. The cavity volume V_c is approximated by that of a spherical cap with a base radius of ρ_c and a height equal to the maximum thermoelastic deformation u_c of the stack when the stress reaches the critical value for crack failure. Combining Eq. (6) with Eqs. (4) and (5) allows a rough estimate of the surface displacement and stress under critical conditions. These quantities are calculated for an inclusion with 10 nm radius, a molar volume of 20 cm^3/mol typical for the materials involved [47], a stack thickness d of 1.5 μm (geometrical thickness for a 40 layer sample) and a critical radius ρ_c of 6.5 μm as extracted from experiment. We find a pressure p_c of 18 kPa, a surface displacement u_c of 34 nm and a critical stress σ_c of 0.52 MPa. The latter value is about three orders of magnitude lower than expected for a bulk crystalline material [48] but still three orders of magnitude above the intrinsic tensile stress expected for the film material [27]. Considering that the oxide films grow with a considerable porosity and the Al_2O_3 additionally with a columnar structure [49] the greatly reduced fracture strength found here seems to be very plausible.

To explain the following steps of crater formation we seek for mechanisms directing fracture along a line forming the crater walls after fracture. On first sight this problem seems to be very similar to that of damage due to a heated inclusion close to the surface where the lines of maximum stress have also been found to have large angles with respect to the surface normal if the distance from the surface is about two times larger than the radius of the inclusion [50]. However, applying the surface inclusion model to the geometry of our problem as found from the above estimates does not yield a reasonable result.

We propose a dynamical model of crater formation based on the assumption of a step-wise stress relaxation in the layer stack including deflections of cracks [51]. As soon as a flaw is formed at the critical radius, the material is locally weakened and fracture first propagates perpendicular to the surface through the first layer. During this propagation the volume of the cavity increases and consequently, the inside pressure and stress will momentarily drop below the critical value for fracture of an intact layer. As soon as the next interface is reached, the line of minimum strength will be the interface; i.e. the crack propagates parallel to the surface creating the first step. During this propagation, i.e. expansion of the cavity, the pressure will according to Eq. (5) decrease further resulting in additional stress relaxation. However, this will be compensated by the reduction of the effective stack thickness due to the cracking of the first layer and, during crack propagation along the interface, cavity radius and stress will rise again. When the stress regains the critical value σ_c the second layer will break and the crack propagates through this layer again perpendicular to the surface. This cycle continues until the crack reaches the surface and the conical cap formed by the step-wise fracture of layers will be ejected. We anticipate that the effective thinning of the stack at the circumference during the formation of the cap results in strong bending and, consequently, delamination of layers in the cap, however, there is no experimental evidence for this additional channel of stress relaxation.

Due to the uncertainty in the absolute amount of deposited energy, the determination of the critical stress σ_c for a layer in the stack is subject to considerable uncertainty. However, it is a major result of the above considerations that this quantity is the important one to determine the radius of the craters and this radius is independent, e.g. from the adhesion strength between layers. This readily explains the equal width of single layer terraces that would otherwise be difficult to interpret in view of the pair-wise adhesion demonstrated in Section 4.1.

6. Correlation of defects with damage

6.1. Experimental strategy

In the previous sections the UV-coatings have been inspected with respect to their content of absorbing defects and the damage phenomena occurring for irradiation with above-threshold fluences of excimer-laser light. It was found that the damage threshold is correlated with both, the residual absorption in the thin film material as well as absorption by thin film defects.

For high quality coatings we expected that the residual absorption of the coating material is so weak that defect absorption would clearly dominate and the onset of damage could unambiguously be attributed to absorbing defects. The measurements described below aimed for a detailed investigation of global and local damage thresholds by the photoacoustic mirage technique and for a direct correlation of photothermally detected defects with damage events.

To accomplish this, high quality samples **F** and **G** were investigated by both techniques. One half of the samples was reserved for a standard photoacoustic mirage measurement to obtain the global damage threshold. In the other half selected areas of about 1 mm^2 area were marked and absorption maps were taken by photothermal displacement scans in these regions. For these scans we used a photothermal apparatus integrated into a commercial metallurgical microscope [52]. Compared to the measurements presented in Section 2 the use of the higher quality optics of the microscope provided not only higher lateral resolution but also a considerable improvement in sensitivity.

Immediately after the photothermal inspection, samples were transferred to the mirage apparatus and the photothermally inspected regions were scanned with successively increased fluences of 248 nm excimer laser light. With this procedure we obtained a low resolution (information averaged over the 100 μm diameter excimer laser spot) map of local damage events. These irradiations were stopped at a fluence level where a number of damage sites could be detected but damage was still very localized. In the final step of investigation the marked sample area was scanned again but this time the intensity of the specular reflex of a HeNe probe beam was monitored. This method of damage detection provides high sensitivity and contrast and a good estimate of the degree of damage and its lateral extension. These damage maps could then be correlated with photothermal images taken at the beginning.

6.2. Global and local damage thresholds

Global damage thresholds were determined by a standard photoacoustic mirage measurement [19]. During irradiation the laser fluence was increased in small steps up to fluences that were about 30% higher than the threshold fluence. By moving the sample after each pulse by a distance larger than the focal diameter of the excimer laser beam each pulse impinged on a surface area that had not been irradiated before. To compensate for local threshold variations, for each fluence mirage amplitude as well as transit time were averaged over ten laser shots. The result of such a measurement for sample **G** is shown in Fig. 10.
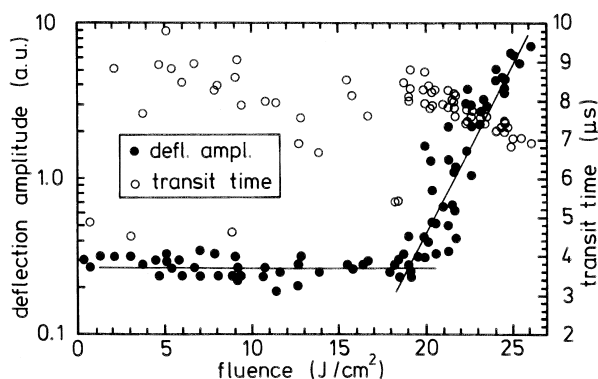
Fig. 10. Fluence-dependent mirage amplitude and transit time for global damage testing on sample **G**.

The graphs for both mirage signal amplitude and transit time show that the signal is below the noise level for fluences below the ablation threshold at 19.0 J/cm^2 and then rises steeply. The fact that below the threshold there is no region with constant transit time and linearly increasing amplitude is a first indication for the defect-induced nature of damage in this sample [19]. For sample **F** we found similar results and extracted a global damage threshold of 22.5 J/cm^2.

For the detection of local damage the marked areas of the samples were irradiated with excimer laser light of a constant intensity within the 100 μm diameter spot on the surface and mirage deflection amplitude and transit time were recorded for each irradiated spot. The procedure was repeated with step-wise increased fluence. To obtain an irradiation as even as possible at the required fluence level, the laser beam was rastered over the surface with partly overlapping irradiations as shown in Fig. 11a. Each mirage scan was performed at a fixed laser fluence starting at about 20% of the damage threshold of the respective coating. During this irradiation sequence each investigated spot was irradiated several times with pulses of increasing fluence. For sample **G** we, e.g. applied fluences of 5.7, 5.8, 6.0, 7.2, 8.3, 8.9, and 9.7 J/cm^2. For this sample first indications for damage could be registered at 8.9 J/cm^2 and scanning was stopped at 9.7 J/cm^2. The mirage amplitude map obtained for sample **G** for this fluence is shown in Fig. 11b. Although the spatial resolution of this image is rather low, it is possible to roughly identify regions with a high damage probability. One major result of these raster damage measurements is the fact that the local damage threshold may differ drastically from the global threshold determined by the experiments described above. Here, global and local damage thresholds differ by more than a factor of two. Careful visual inspection of the rastered surface and the results of HeNe reflectivity scans taken prior to mirage-scanning revealed that most of the severe degradation results from surface contaminants while thin film defects mostly exhibit much weaker effects. Furthermore, it should be mentioned that the raster damage

measurements might be influenced by previously applied irradiation at lower fluence.

6.3. Correlation of damage sites with defects

After the damage scan the marked area on the surface was rastered again. However, during this scan the reflected intensity of a HeNe probe beam was recorded. In the resulting image damage sites can precisely be identified by scattering losses and the decrease in reflected intensity gives a rough estimate of the damage strength. Fig. 12a and b show a comparison of the photothermal scan obtained prior to damaging and the damage map obtained by the reflectivity analysis for sample **G**. It is found that some of the damage sites clearly correlate with defects found in the displacement amplitude image. The corresponding sites are marked by squares in each image.

While the correlation between the marked defects and damage sites is undoubtedly established by the matching locations, we also find numerous defects not leading to damage and on the other hand, damage sites on nominally defect free regions. One reason for the former observation might be the fact that the wavelength utilized for the photothermal inspection was not the same as the damaging wavelength. However, this argument does not seem to be too obvious since we anticipate that any defect absorbing at 514 nm also does so in the UV region. For the weakly absorbing defects the more natural explanation would be that the fluence was just not high enough to cause damage. It is well known that the transfer of pulse laser light energy to defects in thin film systems and following catastrophic damage often cannot simply be treated as a locally increased absorption coefficient but an additional electric field enhancement due to a change in dielectric properties in the vicinity of the defect has to be considered [53,54]. Such a field enhancement, however, will sensitively depend on the specific geometry of the respective defect and its location with respect to the electric field distribution in the film system. Therefore, it is intelligible that defects that exhibit equal absorption strength in the photothermal scan probing the linear absorption properties at 514 nm may be heated very differently by the pulsed laser light at 248 nm. One defect might be buried in a deeper layer or have a different structure or chemical composition than the other.

Another important factor are surface contaminations. Even with careful handling, they are unavoidable if not working in a clean room but in a standard laboratory environment as was the case for all photothermal and damage test experiments introduced here. It was found that surface contaminations produced the strongest photothermal signals and some of them were removed before consecutive analysis. In accordance with observations by other authors [55,56] we also found that contaminations could be removed by sub-threshold irradiation with the excimer laser light. Some of the detected defects might just
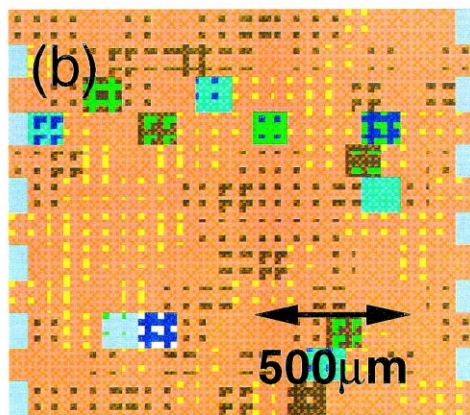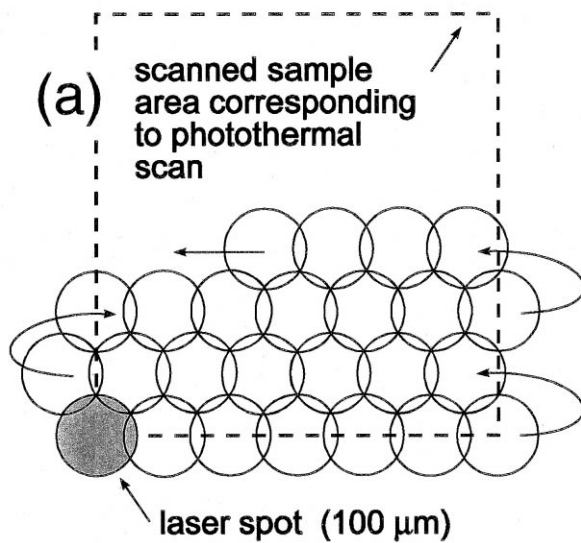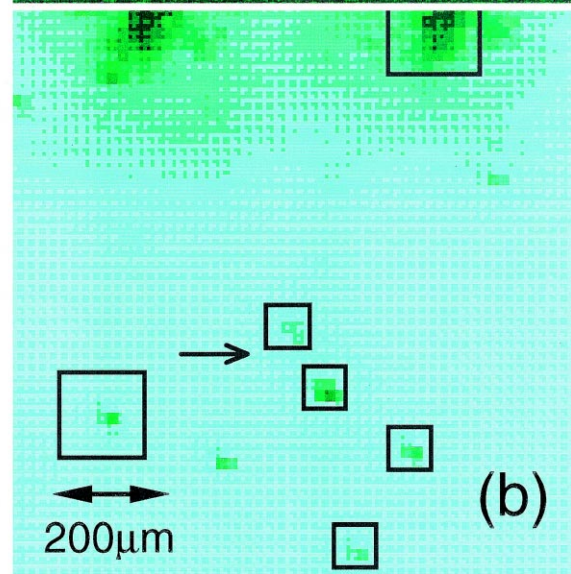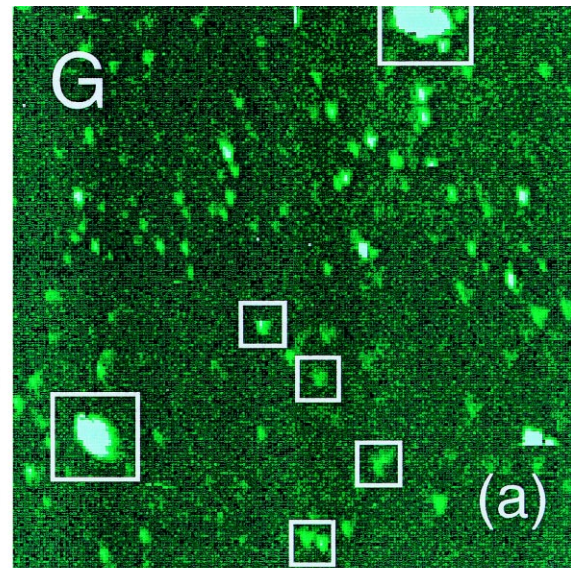
Fig. 11. (a) Raster scan scheme for local damage testing on sample **G**. (b) Mirage amplitude distribution after several raster scans with stepwise increased fluence up to 9.7 J/cm^2.

Fig. 12. (a) Defect distribution obtained from a photothermal scan before local damage testing on sample **G**. (b) Reflectivity image of the sample after local damage testing with fluences up to 9.7 J/cm^2. Squares indicate those locations where a correspondence between photothermally detected defects and damage was found.

have been removed and, therefore, not turned into damaged sites. On the other hand, we observed contaminants appearing between photothermal analysis and the damage experiments. They readily explain that we found severe damage at sites where no defect has been found previously. A prominent example for damage due to surface contaminants are the two extended damage sites in the upper half of Fig. 12b. At the location of the right one, the strongest absorption had been detected in the respective photothermal image (Fig. 12a). We speculate that this absorption was due to a surface contamination and resulted in catastrophic damage during pulsed irradiation. For the

large damage spot on the upper left side, however, we did not find a corresponding absorption in the photothermal scan. Apparently the contamination was attached to the surface between the two measurements. Similar results and features described above have also been found for sample **F**.

To verify the defect- or contamination-related nature of the damage spots, some were inspected by SEM. Two typical examples on sample **G** are shown in Fig. 13. The micrograph in Fig. 13a shows the damage feature marked with an arrow in the damage map of Fig. 12b. Evidently an absorption in the center of the crater was the nucleus of
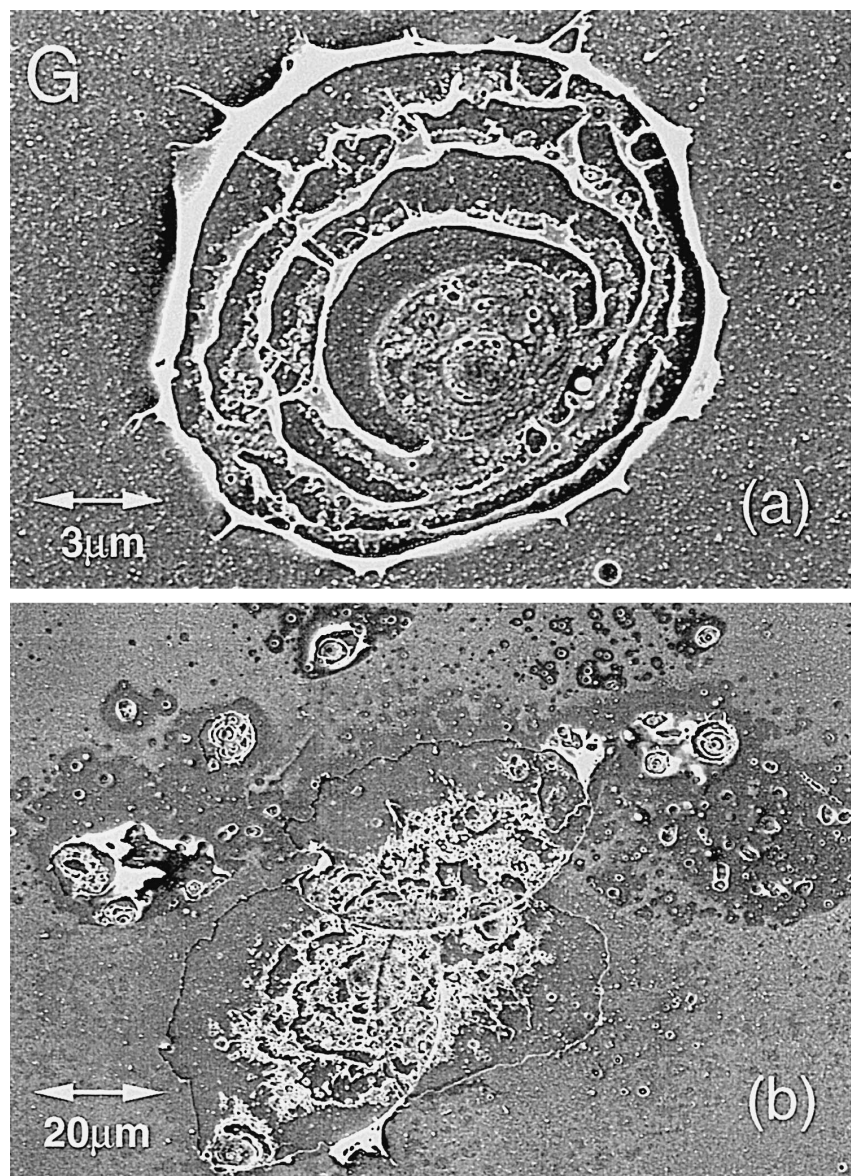
Fig. 13. SEM micrographs of selected regions from Fig. 12b. (a) Damage morphology of the marked spot (→). (b) Large catastrophic failure in the upper right.

damage similar to the features found for the back-side illumination damage of low quality samples (Fig. 8b). However, there are marked differences with respect to crater topography. While in the case of back side illumination we found evidence for elastic failure as the main cause of damage, for the front side-illuminated sample clear indications for melting throughout the film system are found. The damage crater is much less regular and melting pits and droplets are found all over the slopes. Also the absence of a center plateau evidences that in the latter case melting and evaporation are the cause for ablation rather than fracture. This description applies to all front-side illumination craters investigated including, e.g. the small craters found in Fig. 4b. Therefore, we conclude that the result presented in Fig. 13 is not a singular feature

due to the specific defect location of this case but describes the general difference with respect to the electric field distribution compared to the scenario for back-side illumination. While in the latter case only the defect at the interface is strongly heated, for front-side illumination a much higher fluence has to be applied to evaporate a defect buried deep in the layered system. At such high fluence levels not only the defect is evaporated but also the layers above are heated close to the melting point facilitating a plastic deformation of the stack rather than the propagation of cracks along the interfaces.

Fig. 13b, representing the upper right large absorption/damage spot in Fig. 12a and b, is an illustrative example for damage due to surface contamination. Beside a multitude of smaller pits and deep craters we find

large area damage in the form of melting or delamination of one layer or a few layers strongly suggesting that here only the surface is strongly heated. We speculate that the contamination was in form of a fluid or powder and we observe large area damage at locations of high particle concentration while the small pits are a result of local heating due to single particles.

7. Conclusions

Defects play an important role for the UV-laser damage of Al_2O_3/SiO_2 highly reflective coatings. In high quality coatings used for advanced laser applications they, in fact, determine the local damage threshold that may be up to a factor of two below the global threshold found in an averaging standard damage analysis. While most defects seem to be situated at the interface between substrate and thin film system, the most detrimental effects result from damage initiated by surface contaminations.

With photothermal microscopy it is possible to detect and classify defects with respect to their absorption strength and some of them can be directly correlated with damage occurring during UV light irradiation. At present stage a rough classification of the laser resistivity of the coatings based on the defect analysis is possible. However, for a predictive evaluation of damage thresholds based on absorption data more knowledge about the origin and nature of substrate contaminants is required.

Acknowledgements

References

[1] H. Endert, R. Pätzel, D. Basting, Excimer laser: a new tool for precision micromachining, Opt. Quant. Electr. 27 (1995) 1319.

[2] K. Jain, Excimer Laser Lithography, SPIE Optical Engineering Press, Bellingham, 1990.

[3] E. Welsch, Absorption measurements, in: R.E. Hummel, K.H. Guenther (Eds.), Handbook of Optical Properties (Thin films for optical coatings), Vol. I, CRC Press, Boca Raton, 1995, p. 243.

[4] C. Stolz, M.R. Kozlowski, Reduce defects to increase laser damage threshold, Laser Focus World, November 1994.

[5] N. Kaiser, H. Uhlig, U.B. Schallenberg, B. Anton, U. Kaiser, K. Mann, E. Eva, High damage threshold Al_2O_3/SiO_2 dielectric coatings for excimer lasers, Thin Solid Films 260 (1995) 86.

[6] T. Izawa, N. Yamamura, R. Uchimura, I. Hashimoto, T. Yakuoh, Y. Owadano, Y. Matsumoto, M. Yano, Highly damage-resistant reflectors for 248 nm formed by fluoride multilayers, in: H.E. Bennett, L.L. Chase, A.H. Guenther, B.E. Newnam, M.J. Soileau (Eds.), Laser-Induced Damage in Optical Materials: 1990, SPIE Vol. 1441, Bellingham, 1991, p. 339.

[7] A. Bodemann, N. Kaiser, M. Kozlowski, E. Pierce, C. Stolz, Comparison between 355 nm and 1064 nm damage of high grade dielectric mirror coatings, in: H.E. Bennett, A.H. Guenther, M.R. Kozlowski, B.E. Newnam, M.J. Soileau (Eds.), Laser-Induced Damage in Optical Materials: 1995, SPIE Vol. 2714, Bellingham, 1996, p. 395.

[8] E. Welsch, K. Ettrich, H. Blaschke, P. Thomsen-Schmidt, D. Schäfer, N. Kaiser, Investigation of the absorption induced damage in ultraviolet dielectric thin films, Opt. Eng. 36 (2) (1997) 504.

[9] M.R. Kozlowski, R. Chow, The role of defects in laser damage of multilayer coatings, in: H.E. Bennett, L.L. Chase, A.H. Guenther, B.E. Newnam, M.J. Soileau (Eds.), Laser-Induced Damage in Optical Materials: 1993, SPIE Vol. 2114, Bellingham, 1994, p. 640.

[10] M.C. Staggs, M.R. Kozlowski, W.J. Siekhaus, M. Balooch, Correlation of damage threshold and surface geometry of nodular defects in HR coatings as determined by in situ atomic force microscopy, in: H.E. Bennett, L.L. Chase, A.H. Guenther, B.E. Newnam, M.J. Soileau (Eds.), Laser-Induced Damage in Optical Materials: 1992, SPIE Vol. 1848, Bellingham, 1993, p. 234.

[11] M. Commandré, P. Roche, Characterization of optical coatings by photothermal deflection, Appl. Opt. 35 (25) (1996) 5021.

[12] E. Welsch, M. Reichling, Micrometer resolved photothermal displacement inspection of optical coatings, J. Mod. Opt. 40 (8) (1993) 1455.

[13] E. Welsch, Photothermal surface deformation technique—a goal for nondestructive evaluation of thin-film optics, J. Mod. Opt. 38 (11) (1991) 2159.

[14] S. Petzoldt, A.P. Elg, M. Reichling, J. Reif, E. Matthias, Surface laser damage thresholds determined by photoacoustic deflection, Appl. Phys. Lett. 53 (21) (1988) 2005.

[15] M. Reichling, E. Welsch, A. Duparré, E. Matthias, Photothermal absorption microscopy on ZrO_2 and MgF_2 films, Opt. Eng. 33 (4) (1994) 1334.

[16] E. Welsch, H.G. Walther, P. Eckardt, T. Lan, Low-absorption measurement of optical thin films using the photothermal surface-deformation technique, Can. J. Phys. 66 (1988) 638.

[17] P. Zimmermann, D. Ristau, E. Welsch, Potentiality of the photothermal surface-displacement technique for precisely performed absorption measurement of optical coatings, Appl. Phys. A 58 (1994) 377.

[18] K. Mann, E. Eva, A. Hopfmüller, Damage testing and characterization of dielectric coatings for high power excimer lasers, in: F. Abelès (Ed.), Optical Interference Coatings, SPIE Vol. 2253, Bellingham, 1994, p. 731.

[19] M. Reichling, J. Siegel, E. Matthias, H. Lauth, E. Hacker, Photoacoustic studies of laser damage in oxide thin films, Thin Solid Films 253 (1–2) (1994) 333.

[20] K. Mann, H. Gerhardt, Automated damage testing facility for excimer laser optics, in: H.E. Bennett, L.L. Chase, A.H. Guenther, B.E. Newnam, M.J. Soileau (Eds.), Laser-Induced Damage in Optical Materials: 1984, SPIE Vol. 1438, Bellingham, 1985, p. 39.

[21] H. Beyer, Theorie und Praxis der Interferenzmikroskopie, Akademische Verlagsgesellschaft Geest & Portig, Leipzig, 1974.

[22] E. Matthias, J. Siegel, S. Petzoldt, M. Reichling, H. Skurk, O. Käding, E. Neske, In situ investigation of laser ablation of thin films, Thin Solid Films 254 (1995) 139.

[23] A. Bodemann, thesis, Jena Univ., 1992.

[24] Aufdampf-und Zerstäubermaterialien-Verdampferquellen 90/92, Balzers, Liechtenstein, 1992.

[25] K.H. Guenther, H.K. Pulker, Electron microscopic investigations of cross sections of optical thin films, Appl. Opt. 15 (12) (1976) 2992.

[26] H.K. Pulker, K.H. Günther, Elektronenoptische Untersuchung des

Gefüges von aufgedampften Wechselschichtsystemen, Vakuum-Technik 21 (8) (1972) 201.

[27] H.K. Pulker, Mechanical properties of optical thin films, Thin Solid Films 89 (1982) 191.

[28] M.R. Kozlowski, Damage-resistant laser coatings, in: F.R. Flory (Ed.), Thin Films for Optical Systems, Marcel Dekker, New York, 1995.

[29] A. Bodemann, Photothermal defects in high power laser coatings at the limits of detection, Prog. Nat. Sci. 6 (Suppl.) (1996) S–185.

[30] J. Dijon, J. Hue, A. Disgecmez, E. Quesnel, B. Rolland, Thin films laser damage mechanisms at the YAG third harmonic, in: H.E. Bennett, A.H. Guenther, M.R. Kozlowski, B.E. Newnam, M.J. Soileau (Eds.), Laser-Induced Damage in Optical Materials: 1995, SPIE Vol. 2714, Bellingham, 1996, p. 416.

[31] R.W. Hopper, D.R. Uhlmann, Mechanism of inclusion damage in laser glass, J. Appl. Phys. 41 (10) (1970) 4023.

[32] M. Sparks, C.J. Duthler, Theory of infrared absorption and material failure in crystals containing inclusions, J. Appl. Phys. 44 (7) (1973) 3038.

[33] T.W. Walker, A.H. Guenther, P. Nielsen, Pulsed laser-induced damage to thin-film optical coatings: Part II. Theory, IEEE J. Quant. Electron. QE 17 (10) (1981) 2053.

[34] M.L. Scott, A Review of UV Coating Material Properties, NIST Spec. Publ., 688 (1985) 329.

[35] M. Reichling, Z.L. Wu, E. Welsch, D. Schäfer, E. Matthias, High frequency photothermal reflectivity and displacement measurements on thin film samples, in: D. Bicanic (Ed.), Photoacoustic and Photothermal Phenomena III, Springer Series in Optical Sciences, Vol. 69, Springer-Verlag, Berlin, 1992, p. 698.

[36] A.V. Gorbunov, E.M. Nadgornyi, S.N. Vae'kovskii, Laser pulse induced dislocation structure in ionic crystals, Phys. Status Solidi A 66 (1981) 53.

[37] R.W. Hopper, D.R. Uhlmann, Vaporization of inclusions during laser operation, J. Appl. Phys. 41 (13) (1970) 5356.

[38] W. Nowacki, Thermoelasticity, 2nd edn., Pergamon Press, Oxford, 1986, p. 251.

[39] J. Pirot, Mechanical properties of SiO_x thin films, Thin Solid Films 89 (1982) 175.

[40] H. Holleck, Material selection for hard coatings, J. Vac. Sci. Technol. A 4 (1986) 2661.

[41] T.L. Anderson, Fracture Mechanics, 2nd edn., CRC Press, Boca Raton, 1995, p. 38.

[42] F.H. Streitz, J.W. Mintmire, Electrostatic potentials for metal-oxide surfaces and interfaces, Phys. Rev. B 50 (16) (1994) 11996.

[43] S. Baba, A. Kikuchi, A. Kinbara, A microtribometer for measurement of friction and adhesion of coatings, J. Vac. Sci. Technol. A 4 (6) (1986) 3015.

[44] C. Ottermann, Y. Tomita, M. Ishiyama, K. Bange, Influence of aging processes on adhesion properties of metallic and oxidic nthin films, in: S.P. Baker, C.A. Ross, P.H. Townsend, C.A. Volkert, P. Børgsen (Eds.), Thin Films: Stresses and Mechanical Properties V, Mat. Res. Soc. Symp. Proc., Vol. 356, Materials Research Society, Pittsburgh, 1995, p. 839.

[45] K. Mitani, U.M. Gösele, Formation of interface bubbles in bonded silicon wafers: a thermodynamic model, Appl. Phys. A 54 (1992) 543.

[46] H. Leipholz, Theory of Elasticity, Noordhoff International Publishing, Leyden 1974, p. 324.

[47] R.C. Weast (Ed.), Handbook of Chemistry and Physics, 55th edn., CRC Press, Cleveland, 1974.

[48] M.M. Eisenstadt, Introduction to Mechanical Properties, Macmillan, New York, 1971, p. 179.

[49] H.K. Pulker, Coatings on Glass, Elsevier, Amsterdam 1984.

[50] C.J. Duthler, Explanation of laser-damage cone-shaped surface pits, Appl. Phys. Lett. 24 (1) (1974) 5.

[51] Q. Ma, H. Fujimoto, P. Flinn, V. Jain, F. Adibi-Rizi, F. Moghadam, R.H. Dauskardt, Quantitative measurement of interface fracture energy in multi-layer thin film structures, in: A.S. Oates, W.F. Filter, R. Rosenberg (Eds.), Reliability in Microelectronics V, Mat. Res. Soc. Symp. Proc., Vol. 391, Materials Research Society, Pittsburgh, 1995, p. 91.

[52] J. Hartmann, P. Voigt, M. Reichling, Measuring local thermal conductivity in polycrystalline diamond with a high resolution photothermal microscope, J. Appl. Phys. 81 (7) (1997) 2966.

[53] J.F. DeFord, M.R. Kozlowski, Modelling of electric-field enhancement at nodular defects in dielectric mirror coatings, in: H.E. Bennett, L.L. Chase, A.H. Guenther, B.E. Newnam, M.J. Soileau (Eds.), Laser-Induced Damage in Optical Materials: 1992, SPIE Vol. 1848, Bellingham, 1993, p. 455.

[54] V.E. Gruzdev, M.N. Libenson, Electrodynamic instability as a reason for bulk and surface optical damage of transparent media and thin films, in: H.E. Bennett, A.H. Guenther, M.R. Kozlowski, B.E. Newnam, M.J. Soileau (Eds.), Laser-Induced Damage in Optical Materials: 1995, SPIE Vol. 2714, Bellingham, 1996, p. 595.

[55] AC Tam, W.P. Leung, W. Zapka, W. Ziemlich, Laser-cleaning technique for removal of surface particulates, J. Appl. Phys. 71 (7) (1992) 3515.

[56] K. Mann, B. Wolff-Rottke, F. Müller, Removal of dust particles from metal mirror surfaces by excimer laser radiation, in: H.E. Bennett, A.H. Guenther, M.R. Kozlowski, M.J. Soileau (Eds.), Laser-Induced Damage in Optical Materials: 1994, SPIE Vol. 2428, Bellingham, 1995, p. 226.